

# Resonant magnetic X-ray scattering spectra in SDW Cr – *ab initio* study –

Manabu Takahashi

*Faculty of Engineering, Gunma Univ, Kiryu, Gunma 376-8515, Japan*

Jun-Ichi Igarashi

*Faculty of Science, Ibaraki Univ., Mito, Ibaraki 310-8512, Japan*

Kunitomo Hirai

*Department of Physics, Nara Med. Univ., Kashiwara, Nara 634-8521, Japan*

Using *ab-initio* band structure calculation based on the local density approximation, Cr *K*-edge resonant X-ray magnetic scattering spectra are analyzed in the spin density wave (SDW) state of chromium. We perform band structure calculation, assuming an ideal bcc lattice structure with the lattice constant observed at the spin-flip temperature  $T_{\text{SF}}$  and a commensurate SDW state with the propagation vector close to the observed value at  $T_{\text{SF}}$ . Taking account of the spin-orbit interaction, we obtain the orbital moment on each Cr site induced in proportion to the local spin moment, which is quite small, at most a tenth of those in nickel or iron. In spite of the tiny *3d* orbital moment, the orbital polarization is found to have large fluctuations as a function of energy. We obtain the scattering intensity at the Cr *K*-edge on the SDW magnetic Bragg spot, which shows resonant enhancement in good agreement with the experiment. The *3d* orbital polarization is found to be highly correlated with the intensity of the resonant main peak, indicating that the *4p* orbital polarization is mainly induced by the *3d* orbital polarization through the *p-d* hybridization.

## I. INTRODUCTION

Resonant X-ray diffraction technique has attracted much attention in the field of studying spin and orbital properties of the *3d* or *4f* electrons in transition metal or rear-earth metal compounds. Both resonant and non-resonant diffraction techniques have been revealing the charge, spin, orbital and lattice characters in a wide variety of compounds. In particular magnetic diffraction techniques have been applied to various magnetic materials for studying the spin and orbital magnetic properties.<sup>1,2,3,4,5,6,7,8,9,10,11,12,13,14,15,16</sup> In this paper we focus on the magnetic diffraction in the spin density wave in chromium.<sup>4,11</sup>

Chromium is a prototypical itinerant antiferromagnet forming a spin density wave (SDW) state below the Néel temperature. A lot of studies have been carried out for revealing the electronic and magnetic properties of chromium.<sup>4,11,17,18,19</sup> Hill et al.<sup>4</sup> studied the SDW state and the charge density wave (CDW) states by means of the X-ray scattering at the Cr *K*-edge. They estimated the lattice distortion by analyzing the nonresonant intensity, but failed to observe resonant enhancement at the Cr *K*-edge. On the other hand Mannix et al.<sup>11</sup> have successfully observed clear resonant enhancement at the Cr *K*-edge and analyzed the spectra using an atomic model. Noting that the resonant enhancement of the magnetic scattering intensity is mainly caused by the orbital polarization (OP) in the *4p* band,<sup>6,38</sup> it is interesting that a clear resonant peak is observed in spite of the very small orbital moment in the ground state.<sup>11</sup>

We analyze the resonant X-ray magnetic scattering spectra in the SDW chromium, using an *ab initio* band

structure calculation based on the local density approximation (LDA). We cannot rely on the tight-binding model for the *4p* band, because the *4p* wave function is greatly extended in space so that in the crystal most weight of the *4p* wave function is distributed on the neighboring site or interstitial region. We first carry out a conventional band calculation without taking account of the spin-orbit interaction (SOI). We obtain the ground state potential which gives the SDW state, then calculate the wave function in conduction band under the potential. This calculation reproduces the same results as those already reported.<sup>20,21</sup> We take account of the SOI in the final stage. We find that the orbital moment is induced in proportion to the local spin moment on each site, although the orbital moment is as small as a tenth of those in ferromagnetic Fe, Co or Ni.<sup>22,23</sup> It should be noted here that the *3d* OP fluctuates considerably as a function of energy in spite of the tiny orbital moment in the ground state.

Using the wave function thus obtained within the LDA, we calculate the scattering intensity. The calculation reproduces well the photon energy dependence on the SDW Bragg spot and the Fano-type dip in the lower energy side of the resonant main peak.<sup>11</sup> The Fano effect originates from the interference between the amplitudes of the resonant and nonresonant scattering processes. The intensity of the resonant main peak arises from the OP in the *4p* band. In order to clarify how the *4p* OP is induced, we calculate the spectra with turning on and off the SOI selectively in the *3d* and *4p* states. We find that the *4p* OP is induced by the *3d* OP through the *p-d* hybridization, and that the *3d* OP strongly correlates with the resonant peak intensity.

This reminds us of the mechanism of the magnetic circular dichroism (MCD) spectra of X-ray absorption at the transition metal  $K$ -edge. We studied the MCD spectra in Fe, Co, Ni<sup>22,23</sup> and Mn<sub>3</sub>GaC<sup>24</sup>, and revealed that the intensity of the dichroism spectra correlates with the  $3d$  OP through the hybridization between the  $4p$  and  $3d$  states.<sup>22,23,24,25</sup> Also, the sensitivity to electronic states at neighboring sites is closely related to the mechanism of the RXS intensity on the orbital ordering Bragg spot in transition metal compounds. Detailed studies<sup>26,27,28,29,30,31</sup> based on band structure calculations have revealed that the intensity is mainly controlled by the lattice distortion through the hybridization of the transition-metal  $4p$  states and the oxygen  $2p$  states at neighboring sites.

This paper is organized as follows. In the next section, we briefly describe the band structure calculation and the ground state. In Sec. III we formulate the magnetic scattering amplitude. We discuss the photon energy dependence of the scattering intensity and its relation to the electronic states in Sec. IV. The last section is devoted to the concluding remarks.

## II. BAND STRUCTURE CALCULATION

Chromium forms a bcc lattice structure. As cooling its magnetic state turns into a transverse spin density wave (TSDW) state at its Néel temperature  $T_N = 311$  K and into a longitudinal spin density wave (LSDW) state at its spin-flip temperature  $T_{SF} = 122$  K. In the TSDW (LSDW) state, magnetic moments are perpendicular (parallel) to the SDW propagation vector. The wavelength of the SDW is incommensurate with the lattice periodicity.<sup>17</sup> Charge density wave (CDW) and lattice strain wave (LSW) are accompanied by the SDW.<sup>17,18,32,33</sup>

In the present calculation, we assume an ideal bcc lattice structure with the lattice constant  $a = 5.45a_0$ , where  $a_0 = 0.529\text{\AA}$  is Bohr radius. The SDW wavelength is assumed to be  $\lambda_{SDW} = 20a$ , which is very close to the observed value at the spin-flip temperature  $T_{SF}$ . Figure 1 schematically depicts the assumed magnetic structure. For convenience, the coordinate system is chosen such that the  $z$  direction is parallel to the magnetic moment. We first carry out the band calculation self-consistently without the SOI, using the Korringa-Kohn-Rostoker (KKR) method with muffin-tin (MT) approximation. The size of the MT sphere is chosen such that neighboring spheres are touching each other. The maximum number of  $k$  points  $n_k = n_{kx} \times n_{ky} \times n_{kz}$  is  $30 \times 30 \times 2$  in the first Brillouin zone (FBZ) for the LSDW state and  $16 \times 2 \times 16$  for the TSDW state. Then we calculate the eigenvalues and eigenfunctions with adding the SOI term  $\frac{1}{r} \frac{d}{dr} V(r) \ell_z s_z$  to the muffin-tin potential  $V(r)$ . Self-consistent iteration is not carried out. The one electron excited states are calculated up to the energy  $\epsilon_F + 2.0$  ryd, where  $\epsilon_F$  is the Fermi level. We neglect the spin flip

terms  $\ell_+ s_-$  and  $\ell_- s_+$  in the SOI. We expect that the neglected terms cause only minor correction to the OP in transition metals and their compounds.<sup>24,31,34</sup> Since we are dealing with a large unit cell containing 40 inequivalent Cr atoms, this may help us to reduce the calculation volume.

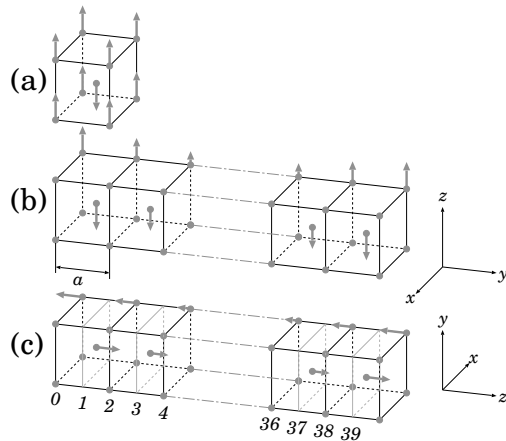


FIG. 1: Schematics of SDW states with  $Q_{SDW} = \frac{2\pi}{a} \frac{19}{20}$ . The arrows represent the direction and the magnitude of magnetic moment. (a) a simple AF states. (b) a TSDW state.  $a$  is the lattice parameter of simple bcc structure. (c) an LSDW state.

We define the spin moment at the  $j$ th site as the difference between electron numbers with spin up and spin down inside the MT sphere placed at the  $j$ th site. That carried by the valence  $d$  electrons  $\mu_{spinj}^d$  is defined as

$$\mu_{spinj}^d = \frac{1}{2} (n_{j\uparrow}^d - n_{j\downarrow}^d), \quad (1)$$

where  $n_{j\alpha}^d$  is the number of spin  $\alpha$  electrons in the  $d$  state inside the  $j$ th MT sphere, and those carried by the valence  $s$  and  $p$  electrons are similarly defined. Another important quantity is the local orbital moment at each site. That carried by the valence  $d$  electrons at the  $j$ th site  $\mu_{orbj}^d$  is defined as

$$\mu_{orbj}^d = \sum_{\alpha} \sum_{m=-2}^2 n_{j\alpha}^{dm} m, \quad (2)$$

where  $m$  represents the magnetic quantum number,  $n_{j\alpha}^{dm}$  is the number of the spin  $\alpha$  electrons in the  $d$  state specified by  $m$  inside the  $j$ th MT sphere. The quantity carried by the valence  $p$  electrons is similarly defined.

Figure 2 shows the distribution of the local spin and orbital moments in the LSDW state. The contributions of the valence  $s$  and  $p$  electrons to the local spin moments are negligible compared with those of the  $d$  electrons. The local orbital moments are also sinusoidally modulated, being proportional to the local spin moment. The magnitude of the local orbital moment is quite small.

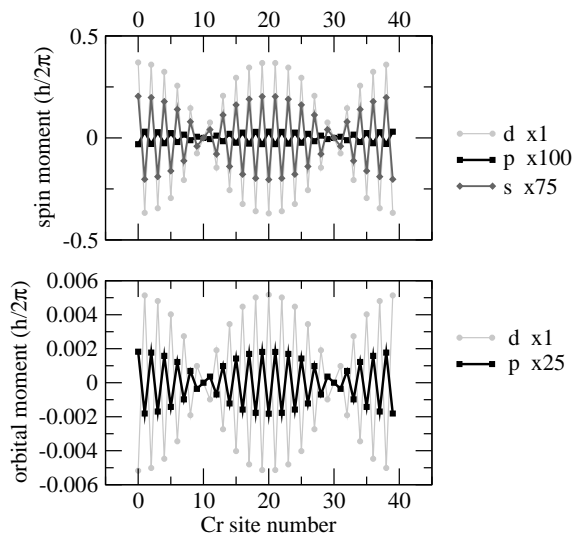


FIG. 2: Spin(upper panel) and orbital(lower panel) moment distribution in LSDW state. The number of  $k$  points in the FBZ is  $16 \times 16 \times 2$ .

The maximum value is about  $0.004\hbar$ , being smaller than a tenth of those in Fe, Co, and Ni.<sup>22,23</sup> Therefore the contribution of the orbital moment to the local moment is negligible. Note that the spin and orbital moment distribution in the TSDW state are nearly the same as those in the LSDW state, except for a slight reduction of the  $p$  orbital moment.

The moments thus obtained may be written as

$$\begin{aligned} \mu_j = & M_1 \cos(\mathbf{Q}_{\text{SDW}} \cdot \boldsymbol{\tau}_j) + M_3 \cos(3\mathbf{Q}_{\text{SDW}} \cdot \boldsymbol{\tau}_j) \\ & + M_5 \cos(5\mathbf{Q}_{\text{SDW}} \cdot \boldsymbol{\tau}_j) + \dots \end{aligned} \quad (3)$$

in terms of the amplitude of the fundamental wave  $M_1$  and the amplitude of the odd-order harmonics  $M_3, M_5, \dots$ , where  $\mathbf{Q}_{\text{SDW}}$  is a propagation vector of the SDW,  $\mathbf{Q}_{\text{SDW}} = \mathbf{Q}_{\text{TSDW}} = \frac{2\pi}{a} (0, \frac{19}{20}, 0)$  for the TSDW state and  $\mathbf{Q}_{\text{SDW}} = \mathbf{Q}_{\text{LSDW}} = \frac{2\pi}{a} (0, 0, \frac{19}{20})$  for the LSDW state.  $\boldsymbol{\tau}_j$  denotes the position vector of the  $j$ th site,  $\boldsymbol{\tau}_j = ja\hat{\mathbf{z}}(\hat{\mathbf{y}})$  for  $n = 0, 2, 4, \dots$  and  $\boldsymbol{\tau}_j = ja\hat{\mathbf{z}}(\hat{\mathbf{y}}) + \frac{1}{2}a(\hat{\mathbf{x}} + \hat{\mathbf{y}} + \hat{\mathbf{z}})$  in the LSDW (TSDW) state. For the  $3d$  spin moments, the coefficients in Eq. (3) are evaluated as  $M_1^{3d} = 0.393\hbar$ ,  $M_3^{3d} = -0.026\hbar$ ,  $M_5^{3d} = 0.0025\hbar$  in the LSDW state. These values are consistent with the reported band calculations<sup>20,21</sup> and the experiment.<sup>11</sup>

The charge density is also modulated, but its magnitude is underestimated compared with the experimental value.<sup>4</sup> If the LSW is taken into account, this drawback may be improved.

Finally in this section, we discuss the partial density of states (PDOS) defined as the density of states projected on the  $p(\ell = 1)$  or  $d(\ell = 2)$  state inside the MT sphere placed at each site. Figure 3 shows those quantities at site  $\boldsymbol{\tau}_0$ , which has the largest magnitude of spin moment. The PDOS in the TSDW state is nearly the same as that in the LSDW state. The PDOS in the previous band

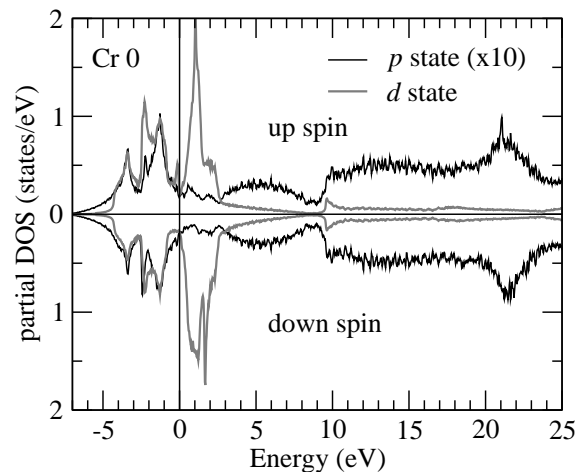


FIG. 3: Partial density of states projected on the MT sphere at  $\boldsymbol{\tau}_0$ . Gray line and black line represent the DOS projected on the  $d$  and  $p$  states, respectively. The number of  $k$  points in the FBZ is  $30 \times 30 \times 2$ . Fermi level  $\epsilon_F$  is at 0 eV

calculation<sup>21</sup> is limited in the energy range  $-7 \sim 5$  eV. The present result is essentially the same as them. The PDOS of the  $p$  state is significantly small compared with that of the  $d$  state. This is consistent with the fact that the wave function of the  $p$  state is greatly extended in space.

### III. MAGNETIC X-RAY SCATTERING SPECTRA

#### A. Formulation

##### 1. nonresonant magnetic scattering

We use the formula given by Blume and Gibbs<sup>3,35</sup> for evaluating the nonresonant magnetic scattering amplitude. The smallness of the orbital angular moment in Cr may allow to ignore the orbital contribution to the scattering amplitude. Then we obtain the expression of the amplitude  $f_{\text{NR}}$  as

$$\begin{aligned} f_{\text{NR}}(\mathbf{q}', \mathbf{e}' \leftarrow \mathbf{q}, \mathbf{e}) \\ = NG(\mathbf{Q}) \sum_j e^{i\mathbf{Q} \cdot \boldsymbol{\tau}_j} f_{\text{NR}}^{\boldsymbol{\tau}_j}(\mathbf{q}', \mathbf{e}' \leftarrow \mathbf{q}, \mathbf{e}), \end{aligned} \quad (4)$$

where

$$\begin{aligned} f_{\text{NR}}^{\boldsymbol{\tau}_j}(\mathbf{q}', \mathbf{e}' \leftarrow \mathbf{q}, \mathbf{e}) = & A \left( -2i \frac{E_{\text{Ryd}}}{\hbar\omega} \right) \\ & \times S_z^{\boldsymbol{\tau}_j}(\mathbf{Q}) \left( \mathbf{e}' \times \mathbf{e} - (\mathbf{e}' \cdot \hat{\mathbf{q}}) (\hat{\mathbf{q}} \times \mathbf{e}) \right. \\ & \left. + (\mathbf{e} \cdot \hat{\mathbf{q}}') (\hat{\mathbf{q}}' \times \mathbf{e}') - (\hat{\mathbf{q}}' \times \mathbf{e}') \times (\hat{\mathbf{q}} \times \mathbf{e}) \right)_z. \end{aligned} \quad (5)$$

Here,  $f_{\text{NR}}^{\boldsymbol{\tau}_j}$  is the scattering amplitude of the atom at  $\boldsymbol{\tau}_j$ , and  $N$  is the number of unit cells in the crystal. Vectors  $\mathbf{q}$

and  $\mathbf{e}$  represent the wave number and polarization of the incident photon, respectively, while  $\mathbf{q}'$  and  $\mathbf{e}'$  are those of the emitted photon. Unit vectors  $\hat{\mathbf{q}}$  and  $\hat{\mathbf{q}}'$  are defined as  $\mathbf{q}/q$  and  $\mathbf{q}'/q'$ , respectively.  $\mathbf{Q}$  is a scattering vector defined by  $\mathbf{q}' - \mathbf{q}$ .  $\hbar\omega$ ,  $E_{\text{Ryd}}$ , and  $mc^2$  represent the photon energy, the energy constant equal to 1 Ryd, and the rest energy of an electron, respectively. Function  $G(\mathbf{Q})$  is defined such that it is unity when  $\mathbf{Q}$  coincides with one of the reciprocal vectors for the SDW supercell, and zero other than the case.  $S_z^{\tau_j}(\mathbf{Q})$  is a Fourier transform of the local spin moment inside the MT sphere at  $\tau_j$ . The direction of magnetization is assumed to be parallel to the  $z$  direction. The factor  $A$  is given by

$$A = \frac{\alpha^2}{4} \left( \frac{\hbar\omega}{E_{\text{Ryd}}} \right)^2, \quad (6)$$

where  $\alpha = \frac{e^2}{\hbar c}$  represents the fine structure constant.

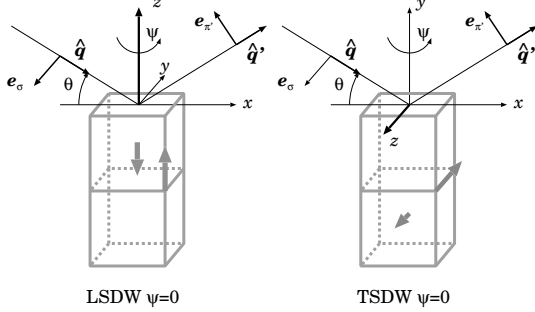


FIG. 4: Scattering geometry for the LSDW(left) and TSDW(right) configuration. Gray arrows represent the direction of the magnetic moment.

In the following, we consider the scattering in the  $\sigma\pi'$  channel with the scattering vector  $\mathbf{Q} = \mathbf{Q}_{\text{LSDW(TSDW)}}$  for the LSDW(TSDW) states. The scattering geometry is defined in Fig. 4. The scattering angle  $\theta$  and azimuthal angle  $\psi$  are shown. The scattering angle is  $\theta \approx 21$  deg. in both of the LSDW and TSDW states. We can easily see that the scattering amplitude for the  $\sigma\sigma'$  channel vanishes in the LSDW state. The amplitude for the  $\sigma\pi'$  channel in the LSDW state is given by

$$\begin{aligned} f_{\text{NR}}(\mathbf{q}', \mathbf{e}' \leftarrow \mathbf{q}, \mathbf{e}) &= A \left( -\frac{2iE_{\text{Ryd}}}{\hbar\omega} \right) 2 \sin^3 \theta \tilde{S}_z(\mathbf{Q}) \\ &\approx -A \frac{i}{110} \sin^3 \theta \tilde{S}_z(\mathbf{Q}), \end{aligned} \quad (7)$$

where

$$\tilde{S}_z(\mathbf{Q}) = \sum_j e^{i\mathbf{Q} \cdot \boldsymbol{\tau}_j} S_z^{\tau_j}(\mathbf{Q}). \quad (8)$$

Here we ignore the photon energy dependence assuming  $\hbar\omega \approx 5990 \text{ eV} \approx 440 E_{\text{Ryd}}$ . Also the amplitude for  $\sigma\pi'$  channel in the TSDW state is given by

$$f_{\text{NR}} \approx -A \frac{i}{110} \sin^2 \theta \cos \theta \sin \psi \tilde{S}_z(\mathbf{Q}). \quad (9)$$

Within the spherical approximation<sup>36</sup>,  $S_z^{\tau_j}(\mathbf{Q})$  is expressed as

$$\begin{aligned} S_z^{\tau_j}(\mathbf{Q}) &= \frac{1}{2} \int_0^{R_{\text{MT}}} \frac{\sin(Qr)}{Qr} r^2 \\ &\quad \times (\rho_{\tau_j \uparrow}(r) - \rho_{\tau_j \downarrow}(r)) dr, \end{aligned} \quad (10)$$

where  $R_{\text{MT}}$  is the radius of the MT sphere and  $\rho_{\tau_j \alpha}(r)$  is the distribution function of the electrons with spin  $\alpha$  inside the MT sphere at  $\tau_j$ . With the help of the band calculation, we evaluate Eq. (10) and thereby Eqs. (7) and (9).

## 2. resonant magnetic scattering

We evaluate the resonant scattering amplitude exploiting the second order Fermi's golden rule.<sup>3,35</sup> We have three terms, the orbital-orbital scattering term  $f_{\text{OO}}$ , the orbital-spin scattering term  $f_{\text{OS}}$ , and the spin-spin scattering term  $f_{\text{SS}}$ .<sup>3,35</sup> Since  $f_{\text{OS}} \sim \left(\frac{\hbar\omega}{mc^2}\right) f_{\text{OO}} \approx f_{\text{OO}} \times 10^{-2}$  and  $f_{\text{SS}} \sim \left(\frac{\hbar\omega}{mc^2}\right)^2 f_{\text{OO}} \approx f_{\text{OO}} \times 10^{-4}$  for the Cr  $K$ -edge,  $f_{\text{OS}}$  and  $f_{\text{SS}}$  can be ignored in the present calculation. We consider only the dipole process, since the quadrupole process gives rise to only minor contribution.

Accordingly the resonant scattering amplitude may be expressed as

$$\begin{aligned} f_{\text{R}}(\mathbf{q}', \mathbf{e}' \leftarrow \mathbf{q}, \mathbf{e}) \\ = NG(\mathbf{Q}) \sum_j e^{i\mathbf{Q} \cdot \boldsymbol{\tau}_j} f_{\text{OO}}^{\tau_j}(\mathbf{q}', \mathbf{e}' \leftarrow \mathbf{q}, \mathbf{e}), \end{aligned} \quad (11)$$

where

$$\begin{aligned} f_{\text{OO}}^{\tau_j}(\mathbf{q}', \mathbf{e}' \leftarrow \mathbf{q}, \mathbf{e}) \\ = \frac{4\pi}{9} \sum_m \sum_{m'} Y_{1m'}(\mathbf{e}') Y_{1m}^*(\mathbf{e}) \\ \times \sum_{n\mathbf{k}\alpha} A' T_{n\mathbf{k}\alpha; \tau_j 1m'\alpha}^\dagger T_{n\mathbf{k}\alpha; \tau_j 1m\alpha} \\ \times \frac{F_{n\mathbf{k}\alpha}^{\tau_j 1m'} F_{n\mathbf{k}\alpha}^{\tau_j 1m*}}{(\hbar\omega - \epsilon_{n\mathbf{k}\alpha} - \epsilon_{1s\alpha} + i\Gamma)/mc^2} \theta(\epsilon_{n\mathbf{k}\alpha} - \epsilon_{\text{F}}), \end{aligned} \quad (12)$$

and

$$F_{n\mathbf{k}\alpha}^{\tau_j \ell m} = \int \psi_{n\mathbf{k}\alpha; \tau_j \ell m}^*(\mathbf{r}) \psi_{n\mathbf{k}\alpha}(\mathbf{r}) d^3r. \quad (13)$$

Here, function  $\theta(x)$  is defined that it is unity when  $x > 0$  and zero other than the case.  $Y_{\ell m}(\mathbf{e})$  is spherical harmonics  $Y_{\ell m}(\theta, \phi)$  with  $e_x = \sin \theta \cos \phi$ ,  $e_y = \sin \theta \sin \phi$ , and  $e_z = \cos \theta$ . Wave function  $\psi_{n\mathbf{k}\alpha}(\mathbf{r})$  is for the state specified by band index  $n$ , wave vector  $\mathbf{k}$ , and spin  $\alpha$  with energy  $\epsilon_{n\mathbf{k}\alpha}$ ; vector  $\mathbf{r}$  represents the relative position from  $\tau_j$ .  $\epsilon_{1s\alpha}$  represent the  $1s$  core level with spin  $\alpha$ , and  $\Gamma$  is the core hole lifetime broadening. Wave function

$\psi_{n\mathbf{k}\alpha;\tau_j\ell m}(\mathbf{r})$  is the projection of  $\psi_{n\mathbf{k}\alpha}(\mathbf{r})$  on the state specified by azimuthal quantum number  $\ell$  and magnetic quantum number  $m$  inside the MT sphere at  $\tau_j$  (it is normalized inside the MT sphere). We write the wave function as

$$\psi_{n\mathbf{k}\alpha;\tau_j\ell m}(\mathbf{r}) = R_{n\mathbf{k}\alpha;\tau_j\ell m\alpha}(r) Y_{\ell m}(\hat{\mathbf{r}}), \quad (14)$$

where  $R_{n\mathbf{k}\alpha;\tau_j\ell m\alpha}(r)$  is the normalized radial wave function.

The dipole transition matrix element  $T_{n\mathbf{k}\alpha;\tau_j1m\alpha}$  is given by

$$\begin{aligned} & T_{n\mathbf{k}\alpha;\tau_j1m\alpha} \\ &= \int_0^{R_{\text{MT}}} R_{n\mathbf{k}\alpha;\tau_j1m\alpha}(r) \frac{r}{a_0} R_{\tau_j1s\alpha}(r) r^2 dr, \end{aligned} \quad (15)$$

where  $R_{\tau_j1s\alpha}(r)$  is the radial wave function of the 1s state with spin  $\alpha$  at  $\tau_j$ . The factor  $A'$  in Eq. (12) is

$$A' = \frac{\alpha^2}{4} \left( \frac{\epsilon_{n\mathbf{k}\alpha} - \epsilon_{1s}}{E_{\text{Ryd}}} \right)^2. \quad (16)$$

Since  $\hbar\omega \approx \epsilon_{n\mathbf{k}\alpha} - \epsilon_{1s}$ , this factor nearly equal to the factor  $A$  in the nonresonant scattering amplitude. Hereafter, we replace  $A'$  by  $A$ .

We rewrite the site scattering factor  $f_{\text{OO}}^{\tau_j}$  as

$$\begin{aligned} & f_{\text{OO}}^{\tau_j}(\mathbf{q}', \mathbf{e}' \leftarrow \mathbf{q}, \mathbf{e}) \\ &= A \frac{4\pi}{9} \sum_m \sum_{m'} Y_{1m'}(\mathbf{e}') Y_{1m}^*(\mathbf{e}) \\ &\times \int_{-\infty}^{\infty} d\epsilon \frac{\rho_{m'm}^{\tau_j}(\epsilon)}{(\hbar\omega - \epsilon - \epsilon_{1s\alpha} + i\Gamma)/mc^2} \theta(\epsilon - \epsilon_{\text{F}}), \end{aligned} \quad (17)$$

where the dipole transition density matrix  $\rho_{m'm}^{\tau_j}(\epsilon)$  is defined by

$$\begin{aligned} \rho_{m'm}^{\tau_j}(\epsilon) &= \sum_{\alpha n\mathbf{k}} T_{n\mathbf{k}\alpha;\tau_j1m'\alpha}^\dagger T_{n\mathbf{k}\alpha;\tau_j1m\alpha} \\ &\times F_{n\mathbf{k}\alpha}^{\tau_j1m'} F_{n\mathbf{k}\alpha}^{\tau_j1m*} \delta(\epsilon - \epsilon_{n\mathbf{k}\alpha}). \end{aligned} \quad (18)$$

Incidentally, the absorption intensity  $I_{\text{abs}}$  in the dipole process may be given by

$$I_{\text{abs}} \sim -\Im \sum_{jm} \int_{-\infty}^{\infty} d\epsilon \frac{\rho_{mm}^{\tau_j}(\epsilon)}{(\hbar\omega - \epsilon - \epsilon_{1s\alpha} + i\Gamma)/mc^2}, \quad (19)$$

where  $\Im A$  stands for the imaginary part of  $A$ .

The matrix  $\rho_{m'm}^{\tau_j}(\epsilon)$  bears the symmetry compatible with the LSDW or TSDW states. Let  $\rho^{\tau_j}(\epsilon)$  be

$$\rho^{\tau_j}(\epsilon) = \begin{pmatrix} a & \alpha & \gamma \\ \alpha^* & b & \beta \\ \gamma^* & \beta^* & c \end{pmatrix}. \quad (20)$$

Then  $\rho^{\tau_j+10a\hat{z}(\hat{y})}(\epsilon)$  has to be

$$\rho^{\tau_j+10a\hat{z}(\hat{y})}(\epsilon) = \begin{pmatrix} c & -\beta^* & \gamma^* \\ -\beta & b & -\alpha^* \\ \gamma & -\alpha & a \end{pmatrix}, \quad (21)$$

in the LSDW(TSDW) state with  $Q_{\text{LSDW(TSDW)}} = \frac{2\pi}{a} \frac{19}{20}$ . Note that the off-diagonal elements  $\alpha$ ,  $\beta$  and  $\gamma$  are zero in the LSDW state, because of the four fold rotational symmetry along the  $z$  direction. In the TSDW state, this symmetry is not hold in a strict sense. However, one may expect that it is approximately hold, because the wave length of the SDW is quite long  $\lambda_{\text{SDW}} = 20a$ , leading to very small off-diagonal elements in the transition density matrix.

The scattering amplitude for the resonant process may be rewritten as

$$\begin{aligned} & f_{\text{R}}(\mathbf{q}', \mathbf{e}' \leftarrow \mathbf{q}, \mathbf{e}) \\ &= \frac{4\pi}{9} ANG(\mathbf{Q}) \sum_{m'm} Y_{1m'}(\mathbf{e}') Y_{1m}^*(\mathbf{e}) \\ &\times \int_{-\infty}^{\infty} d\epsilon \frac{\tilde{\rho}_{m'm}(\epsilon, \mathbf{Q})}{(\hbar\omega - \epsilon - \epsilon_{1s\alpha} + i\Gamma)/mc^2} \theta(\epsilon - \epsilon_{\text{F}}), \end{aligned} \quad (22)$$

where

$$\tilde{\rho}(\epsilon, \mathbf{Q}) = \sum_j e^{-i\mathbf{Q}\cdot\tau_j} \rho^{\tau_j}(\epsilon). \quad (23)$$

Then  $\tilde{\rho}(\epsilon, \mathbf{Q})$  has the form

$$\tilde{\rho}(\epsilon, \mathbf{Q}) = \begin{pmatrix} \xi & \eta & \zeta \\ \eta^* & 0 & \eta^* \\ \zeta^* & \eta & -\xi \end{pmatrix}. \quad (24)$$

From the above-mentioned symmetry argument on  $\rho^{\tau_j}(\epsilon)$ , the off-diagonal elements  $\eta, \zeta$  are zero in the LSDW state. The scattering amplitude for the  $\sigma\pi'$  channel in the LSDW state becomes

$$\begin{aligned} & f_{\text{R}}(\mathbf{q}', \mathbf{e}^{\pi'} \leftarrow \mathbf{q}, \mathbf{e}^{\sigma}) = -\frac{1}{3} ANG(\mathbf{Q}) i \sin \theta \\ &\times \int_{-\infty}^{\infty} d\epsilon \frac{\xi(\epsilon, \mathbf{Q})}{(\hbar\omega - \epsilon - \epsilon_{1s\alpha} + i\Gamma)/mc^2}. \end{aligned} \quad (25)$$

It is easily seen that the amplitude for the  $\sigma\sigma'$  channel is zero. Also, in the TSDW state, the off-diagonal elements  $\eta, \zeta$  are expected to be very small. Neglecting them, we obtain the scattering amplitude for the  $\sigma\pi'$  channel in the TSDW state as

$$\begin{aligned} & f_{\text{R}}(\mathbf{q}', \mathbf{e}^{\pi'} \leftarrow \mathbf{q}, \mathbf{e}^{\sigma}) = \frac{1}{6} ANG(\mathbf{Q}) i \\ &\times \int_{-\infty}^{\infty} d\epsilon \left[ \frac{(2\xi - \zeta + \zeta^*) \cos \theta \sin \psi}{(\hbar\omega - \epsilon - \epsilon_{1s\alpha} + i\Gamma)/mc^2} \right. \\ &\quad \left. - \frac{\sqrt{2}(\eta + \eta^*) \cos \theta \cos \psi}{(\hbar\omega - \epsilon - \epsilon_{1s\alpha} + i\Gamma)/mc^2} \right] \theta(\epsilon - \epsilon_{\text{F}}) \\ &\approx \frac{1}{3} ANG(\mathbf{Q}) i \cos \theta \sin \psi \\ &\times \int_{-\infty}^{\infty} d\epsilon \frac{\xi(\epsilon, \mathbf{Q})}{(\hbar\omega - \epsilon - \epsilon_{1s\alpha} + i\Gamma)/mc^2}. \end{aligned} \quad (26)$$

The amplitude in the  $\sigma\sigma'$  is zero if the off-diagonal elements  $\eta$ ,  $\zeta$  are zero.

Using the non-resonant and resonant scattering amplitude thus obtained, the scattering cross section can be written as,

$$\frac{d\sigma}{d\Omega} = r_e^2 |f_{\text{NR}} + f_{\text{R}}|^2, \quad (27)$$

where  $r_e = \frac{e^2}{mc^2}$  represents the classical electron radius.

## IV. RESULTS AND DISCUSSION

### Absorption spectra

At present, it is difficult to estimate accurately the  $1s$  core level  $\epsilon_{1s}$  and the core-hole lifetime broadening  $\Gamma$  from the calculation. We adjust these values such that the calculated  $K$ -edge absorption intensity reproduces the photon energy dependence observed in the experiment.<sup>11</sup> We calculate the spectra using Eq. (19), assuming that  $\epsilon_{1s} = \epsilon_{\text{F}} - 5988.4\text{eV}$  and  $\Gamma = 0.6 \sim 1\text{eV}$ . Figure 5 shows the calculated absorption spectra in comparison with the experiment. The calculated spectral shape is roughly proportional to the PDOS for the unoccupied  $4p$  state. The calculated curves agree well with the experiment except for a shape around  $\hbar\omega = 6010\text{eV}$ . The peak around  $6010\text{eV}$  comes from the peak around  $21\text{eV}$  in the  $p$  PDOS. Note that no noticeable difference is found between the LSDW and TSDW states. This good agreement between the calculation and the experiment may justify the neglect of the core-hole potential in the calculation of resonant scattering spectra.

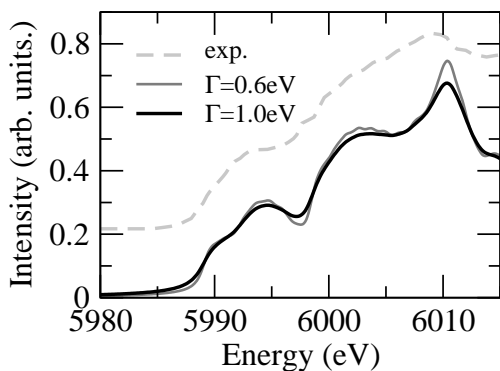


FIG. 5: Comparison of the absorption spectra. Solid and broken lines represent the calculated spectra and experiment.  $1s$  core level is assumed to be  $\epsilon_{1s} = \epsilon_{\text{F}} - 5988.4\text{eV}$ . The lifetime broadening of the intermediate states is assumed to be  $\Gamma = 0.6\text{eV}$  and  $1.0\text{eV}$ .

### magnetic scattering spectra

Putting  $\Gamma = 0.6\text{eV}$  and using the same values of  $\epsilon_{1s}$  as in the absorption spectra, we calculate the magnetic scattering spectra. We first check the convergence of the spectral curve with varying number of  $k$ -points  $n_k$  in the FBZ. Figure 6 shows the spectral curves calculated with three values of  $n_k$  at  $\mathbf{Q} = \mathbf{Q}_{\text{LSDW}}$  in the LSDW state. The spectra calculated at  $\hbar\omega > 6000\text{eV}$  show strong dependence on  $n_k$ , no sign of convergence even for  $n_k = 30 \times 30 \times 2$ . On the other hand, the curve around  $\hbar\omega = 5990\text{eV}$  depends little on  $n_k$ , suggesting a convergence even for  $n_k = 12 \times 12 \times 2$ .

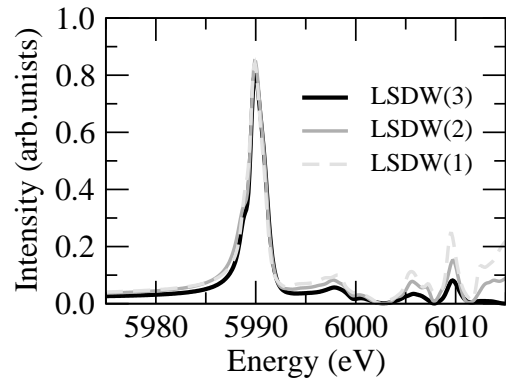


FIG. 6: Convergence of the scattering intensity at  $\mathbf{Q} = \mathbf{Q}_{\text{LSDW}}$  for LSDW state against the number of  $k$ -points. The number of  $k$ -points are  $12 \times 12 \times 2$ ,  $16 \times 16 \times 2$  and  $30 \times 30 \times 2$  for LSDW(1), LSDW(2) and LSDW(3), respectively. The  $1s$  core level and the lifetime broadening assumed to be  $\epsilon_{1s} = \epsilon_{\text{F}} - 5988.4\text{eV}$  and  $\Gamma = 0.6\text{eV}$ , respectively.

Figure 7 shows the calculated spectral curves in the LSDW and TSDW states, in comparison with the experiment<sup>11</sup>. The absorption correction is not made in the experimental curves. The calculation reproduces successfully not only the Fano-type dip around  $\hbar\omega = 5986\text{eV}$  in the TSDW state but also the resonant behavior in good agreement with the experiment.

The resonant intensity arises from the OP in the  $4p$  bands. In order to clarify how the OP is induced, we investigate the change of the electronic states by turning on and off the SOI on the  $p$  and  $d$  states selectively. Figure 8 shows the density of OP  $\mu_{\ell}^{\tau_0}(\epsilon)$  as a function of energy in the LSDW state. This quantity is defined as

$$\mu_{\ell}^{\tau_0}(\epsilon) = \sum_{m=-\ell}^{\ell} m \rho_{\ell m}^{\tau_0}(\epsilon), \quad (28)$$

where  $\rho_{\ell m}^{\tau_0}(\epsilon)$  is the partial DOS projected on the state specified by azimuthal quantum number  $\ell$  and magnetic quantum number  $m$  inside the MT sphere at site  $\tau_0$ . (The site  $\tau_0$  has the largest magnetic moment.) When the SOI is working on both the  $p$  and  $d$  states (panel a),  $\mu_2^{\tau_0}(\epsilon)$  for the  $d$  states is quite large for  $0 \lesssim \epsilon \lesssim 2\text{eV}$  but

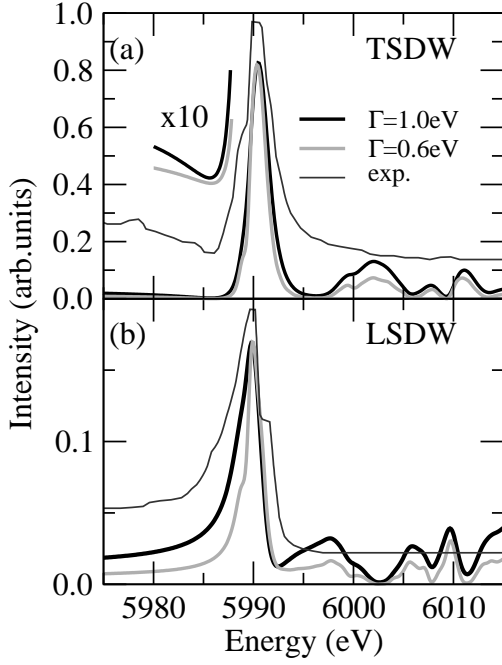


FIG. 7: (a) Calculated magnetic scattering intensities for  $\sigma\pi'$  channel on the SDW Bragg spots  $\mathbf{Q}_{\text{TSDW}}$  in the TSDW state. The azimuthal angle is assumed to be  $\psi = 90$  deg. (b) Those on the spot  $\mathbf{Q}_{\text{LSDW}}$  in the LSDW state. The number of  $k$  points in FBZ is  $n_k = 16 \times 16 \times 2$ . The azimuthal angle is assumed to be  $\psi = \frac{\pi}{2}$  for the TSDW state.  $1s$  core level is assumed to be  $\epsilon_{1s} = \epsilon_F - 5988.4$  eV. Both results with  $\Gamma = 0.6$  eV and  $\Gamma = 1.0$  eV are shown for comparison. The spectra with  $\Gamma = 1.0$  eV is normalized so that the peak height at 5990 eV is equal with that of the spectra with  $\Gamma = 0.6$  eV. The experiment curve is traced from Ref.<sup>11</sup>.

nearly zero for  $\epsilon \gtrsim 3$  eV.  $\mu_1^{\tau_0}(\epsilon)$  for the  $p$  states is smaller in two order of magnitude than  $\mu_2^{\tau_0}(\epsilon)$ . When the  $d$  SOI is turned off but the  $p$  SOI is still turned on (panel b),  $\mu_2^{\tau_0}(\epsilon)$  becomes very small in the whole energy range. Corresponding to this change,  $\mu_1^{\tau_0}(\epsilon)$  also becomes very small for  $0 \lesssim \epsilon \lesssim 5$  eV, although it does not change for  $\epsilon \gtrsim 5$  eV from the values in the case when both of the  $p$  and  $d$  SOI's are turned on. When only the  $p$  SOI is turned off but the  $d$  SOI is turned on (panel c),  $\mu_2^{\tau_0}(\epsilon)$  is essentially unchanged in the whole energy range from the value in the case when both of the  $p$  and  $d$  SOI's are turned on.  $\mu_1^{\tau_0}(\epsilon)$  changes little for  $\epsilon \lesssim 5$  eV, but it is considerably reduced for  $\epsilon \gtrsim 10$  eV.

These results clearly indicate that the  $p$  OP for  $0 \lesssim \epsilon \lesssim 5$  eV is mainly induced by the  $d$  OP through the  $p$ - $d$  hybridization. Since the  $d$  DOS is concentrated in  $\epsilon \lesssim 2$  eV, the hybridization with the  $p$  states at neighboring site may be effective only for  $\epsilon \lesssim 2$  eV. The effect of the  $p$  SOI on the  $p$  OP seems to be reduced by this hybridization. Note that the  $p$  and  $d$  states do not hybridize each other at the same site because the SDW wavelength is so long that each site almost keeps the inversion symmetry, particularly at  $\tau_0$ . The  $p$  OP for  $\epsilon \gtrsim 10$  eV is

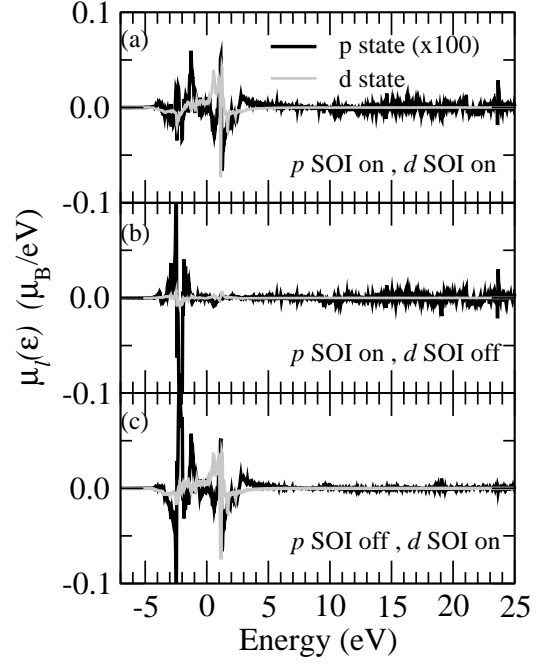


FIG. 8: Orbital moment densities  $\mu_1^{\tau_j}(\epsilon)$  and  $\mu_2^{\tau_j}(\epsilon)$  on the site at  $\tau_0$ . (a) Both of the  $p$  SOI and  $d$  SOI are turned on. (b) The  $d$  SOI is turned off. (c) The  $p$  SOI is turned off. Solid line and gray line represent the orbital density for the  $p$  state  $\mu_1^{\tau_j}(\epsilon)$  and  $d$  symmetric states  $\mu_2^{\tau_j}(\epsilon)$ , respectively. The orbital density for the  $p$  states is multiplied by 100. The number of  $k$ -points in FBZ is  $30 \times 30 \times 2$ .

mainly induced by the  $p$  SOI.

Since the resonant intensity arises from the  $p$  OP, the above finding that the  $p$  OP for  $\epsilon \lesssim 5$  eV is induced by the  $d$  OP through the  $p$ - $d$  hybridization may be confirmed by calculating directly the spectra with turning on and off the  $p$  SOI and  $d$  SOI. Figure 9 shows the calculated results. When only the  $d$  SOI is turned off, the resonant main peak at  $\hbar\omega = 5990$  eV disappears, while the resonant structures for higher energies change little. On the other hand, when only the  $p$  SOI is turned off, the main peak dose not change, while the resonant structure for higher energies almost disappears. This SOI dependence of the spectra corresponds well to the SOI dependence of the  $p$  OP. Consequently, it is conclude that the resonant main peak at  $\hbar\omega = 5990$  eV strongly correlates with the  $3d$  states.

Finally we discuss the origin of the Fano-type dip. Since the Fano effect arises from the interference between the non-resonant and resonant terms, we look into  $f_{\text{NR}}$  and  $f_{\text{R}}$ , which are shown in Fig. 10.  $f_{\text{NR}}$  is purely imaginary. Note that  $f_{\text{R}}$  in the LSDW state is nearly proportional to that in the TSDW state with reverse sign. The reverse sign arises from the difference of the scattering geometry in the LSDW and TSDW states. As a result, in the TSDW state, the imaginary part of  $f_{\text{R}}$  and  $f_{\text{NR}}$  can be canceled at  $\hbar\omega \approx 5987$  eV, with a small real part

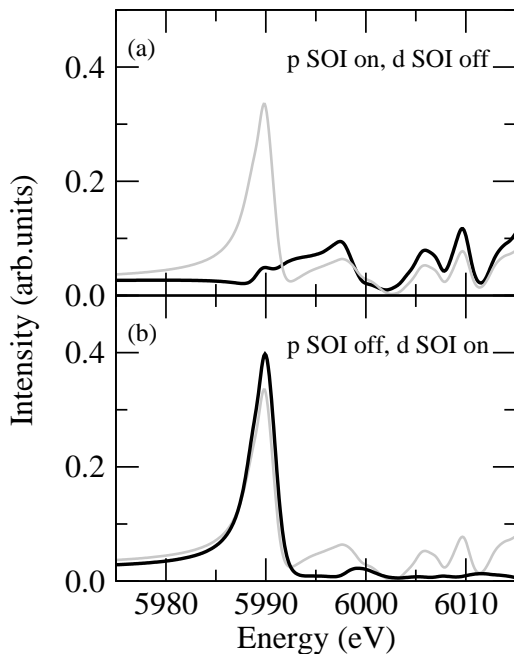


FIG. 9: Scattering intensity on the SDW spot  $\mathbf{Q}_{\text{LSDW}}$  in LSDW state. (a) The SOI in  $p$  state is turned on and the SOI in  $d$  state is turned off. (b) The SOI in  $p$  state is turned off and the SOI in  $d$  state is turned on. The  $1s$  core level is assumed as  $\epsilon_{1s} = \epsilon_F - 5988.4$  eV. The gray line is shown for comparison, which is calculated with both of the  $p$  SOI and  $d$  SOI being turned on.

of  $f_R$ . This is the reason why the Fano dip is seen at  $\hbar\omega \approx 5987$  eV. On the other hand, one can easily see that such a cancellation is hard in the LSDW state.

## V. CONCLUDING REMARKS

We have performed an *ab initio* band structure calculation based on the LDA with a large unit cell. Assuming that the potential has a modulation with  $Q_{\text{SDW}} = \frac{2\pi}{a} \frac{19}{20}$ , we reproduced well the SDW state previously reported.<sup>20,21</sup> Since the orbital momentum is essential to the resonant magnetic scattering, we have taken account of the SOI within the  $\ell_z s_z$  approximation. The orbital magnetic moment is mainly induced on the  $3d$  states in proportion to the spin magnetic moment at each Cr site.

We have calculated the absorption spectra at the Cr  $K$ -edge. The dipole matrix elements are evaluated by using the wave functions obtained from the band structure calculation. Having neglected the core-hole potential, we have obtained the absorption spectra in good agreement with the experiment.<sup>11</sup> This may justify neglecting the core-hole potential in the calculation of the resonant magnetic scattering spectra.

We have calculated the resonant x-ray magnetic scattering spectra on the SDW magnetic Bragg spot in the TSDW and LSDW states. A resonant enhancement has

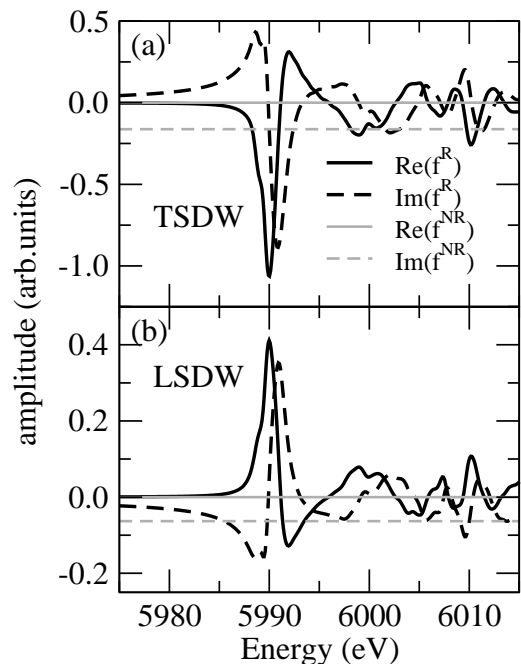


FIG. 10: (a) Scattering amplitudes on the spot  $\mathbf{Q}_{\text{TSDW}}$  for the TSDW state. (b) Those on the spot  $\mathbf{Q}_{\text{LSDW}}$  for the LSDW state. Solid and broken lines represent the real and imaginary part of the amplitude due to the resonant scattering, respectively. Thin broken line represents the imaginary part of the amplitude due to the nonresonant scattering. The real part of the nonresonant contributions is zero.  $\epsilon_{1s} = \epsilon_F - 5988.4$  eV and  $\Gamma = 1.0$  eV.

been reproduced near the  $K$ -edge in good agreement with the experiment.<sup>11</sup> In the TSDW state, the off-diagonal matrix elements of the scattering amplitude have been neglected, since they are expected to be small from a symmetry argument. Experiments on the azimuthal angle dependence of the resonant intensity may help us check the accuracy of the argument.

The mechanism of the resonant magnetic scattering has been clarified. We found that the OP on the  $3d$  states fluctuates considerably as a function of energy, although the local orbital magnetic moment in the  $d$  states is quite small. This  $d$  OP induces the  $p$  OP around the Fermi level through the  $p$ - $d$  hybridization, and thereby gives rise to the resonant scattering intensity. The resonant main peak at  $\hbar\omega = 5990$  eV strongly correlates with the  $3d$  states. This finding is consistent with the analysis<sup>37</sup> of the resonant magnetic scattering of  $\text{UGa}_3$ <sup>12</sup>, where a large signal is found at the Ga  $K$ -edge. This is interpreted as a reflection of the large OP on the uranium  $5f$  states.

We have reproduced a Fano-type dip at  $\hbar\omega \approx 5987$  eV in the TSDW state.<sup>11</sup> The Fano-type dip is seen only in the TSDW state. This difference arises from the sign of the resonant scattering amplitude (the energy dependence of the amplitude is nearly the same in the two states except for the sign), owing to the different scatter-



ing geometry.

Finally we comment on the CDW state. The assumption of an ideal bcc lattice gives rise to only a small CDW amplitude. The LSW may be dispensable for obtaining a sufficient magnitude of the CDW amplitude. A detailed study on the CDW state is left in future.

### Acknowledgments

This research was partially supported by the Ministry of Education, Science, Sports and Culture, Japan,

Grant-in-Aid for Young Scientists (B), 15740196, 2003 and Grant-in-Aid for Scientific Research (C)(2).

- 
- <sup>1</sup> F. de Bergevin and M. Brunel, *Acta Crystallogr., Sect. A: Cryst. Phys., Diff., Theor. Gen. Crystallogr.* **37**, 324 (1981).
  - <sup>2</sup> K. Namikawa, T. Nakajima, and K. Kowata, *J. Phys. Soc. Jpn.* **54**, 4099 (1985).
  - <sup>3</sup> M. Blume and D. Gibbs, *Phys. Rev. B* **37**, 1779 (1988).
  - <sup>4</sup> J. P. Hill, C.-C. Kao, and D. F. McMorrow, *Phys. Rev. B* **55**, R8662 (1997).
  - <sup>5</sup> D. Gibbs, D. R. Harshman, E. D. Isaacs, D. B. McWhan, D. Mills, and C. Vettier, *Phys. Rev. Lett.* **61**, 1241 (1988).
  - <sup>6</sup> J. P. Hannon, G. T. Trammell, M. Blume, and D. Gibbs, *Phys. Rev. Lett.* **61**, 1245 (1988).
  - <sup>7</sup> P. Carra, M. Altarelli, and F. de Bergevin, *Phys. Rev. B* **40**, 7324 (1989).
  - <sup>8</sup> W. Neubeck, C. Vettier, K.-B. Lee, and F. de Bergevin, *Phys. Rev. B* **60**, R9912 (1999).
  - <sup>9</sup> A. Stunault, F. de Bergevin, D. Wermeille, C. Vettier, T. Brückel, N. Bernhoeft, G. J. McIntyre, and J. Y. Henry, *Phys. Rev. B* **60**, 10170 (1999).
  - <sup>10</sup> W. Neubeck, C. Vettier, F. de Bergevin, F. Yakhov, D. Mannix, O. Bengone, M. Alouani, and A. Barbier, *Phys. Rev. B* **63**, 134430 (2001).
  - <sup>11</sup> D. Mannix, P. C. de Camargo, C. Giles, A. J. A. de Oliveira, F. Yokaichiya, and C. Vettier, *Eur. Phys. J. B* **20**, 19 (2001).
  - <sup>12</sup> D. Mannix, A. Stunault, N. Bernhoeft, L. Paolasini, G. H. Lander, C. Vettier, F. deBergevin, D. Kaczorowski, and A. Czopnik, *Phys. Rev. Lett.* **86**, 4128 (2001).
  - <sup>13</sup> R. Caciuffo, L. Paolasini, A. Sollier, P. Ghigna, E. Pavarini, J. van den Brink, and M. Altarelli, *Phys. Rev. B* **65**, 174425 (2002).
  - <sup>14</sup> L. Paolasini, R. Caciuffo, A. Sollier, P. Ghigna, and M. Altarelli, *Phys. Rev. Lett.* **88**, 106403 (2002).
  - <sup>15</sup> S. B. Wilkins, P. D. Hatton, M. D. Roper, D. Prabhakaran, and A. T. Boothroyd, *Phys. Rev. Lett.* **90**, 187201 (2003).
  - <sup>16</sup> M. van Veenendaal, *Phys. Rev. B* **67**, 134112 (2003).
  - <sup>17</sup> E. Fawcett, *Rev. Mod. Phys.* **60**, 209 (1988).
  - <sup>18</sup> M. Mori and Y. Tsunoda, *J. Phys. C* **5**, L77 (1993).
  - <sup>19</sup> P. G. Evans, E. D. Isaacs, G. Aeppli, Z. Cai, and B. Lai, *Science* **295**, 1042 (2002).
  - <sup>20</sup> K. Hirai, *J. Phys. Soc. Jpn.* **67**, 1776 (1998).
  - <sup>21</sup> R. Hafner, D. Spišák, R. Lorenz, and J. Hafner, *Phys. Rev. B* **65**, 184432 (2002).
  - <sup>22</sup> J. Igarashi and K. Hirai, *Phys. Rev. B* **50**, 17820 (1994).
  - <sup>23</sup> J. Igarashi and K. Hirai, *Phys. Rev. B* **53**, 6442 (1996).
  - <sup>24</sup> M. Takahashi and J. Igarashi, *Phys. Rev. B* **67**, 245104 (2003).
  - <sup>25</sup> J. P. Rueff, R. M. Galéra, C. Giorgetti, E. Dartyge, C. Brouder, and M. Alouani, *Phys. Rev. B* **58**, 12271 (1998).
  - <sup>26</sup> I. S. Elfimov, V. I. Anisimov, and G. A. Sawatzky, *Phys. Rev. Lett.* **82**, 4264 (1999).
  - <sup>27</sup> M. Benfatto, Y. Joly, and C. R. Natoli, *Phys. Rev. Lett.* **83**, 636 (1999).
  - <sup>28</sup> M. Takahashi, J. Igarashi, and P. Fulde, *J. Phys. Soc. Jpn.* **68**, 2530 (1999).
  - <sup>29</sup> M. Takahashi and J. Igarashi, *Phys. Rev. B* **64**, 075110 (2001).
  - <sup>30</sup> M. Takahashi and J. Igarashi, *Phys. Rev. B* **65**, 205114 (2002).
  - <sup>31</sup> M. Takahashi, M. Usuda, and J. Igarashi, *Phys. Rev. B* **67**, 064425 (2003).
  - <sup>32</sup> R. Pynn, W. Press, S. M. Shapiro, and S. A. Werner, *Phys. Rev. B* **13**, 295 (1976).
  - <sup>33</sup> J. P. Hill, G. Helgesen, and D. Gibbs, *Phys. Rev. B* **51**, 10336 (1995).
  - <sup>34</sup> M. Usuda, M. Takahashi, and J. Igarashi, *Phys. Rev. B* **69**, 014408 (2004).
  - <sup>35</sup> M. Blume, *J. Appl. Phys.* **57**, 3615 (1985).
  - <sup>36</sup> P. Coppens, Z. Su, and P. J. Becker, *International Tables for Crystallography* (Kluwer Academic, BOSTON, 1999), vol. C, chap. Analysis of charge and spin densities, pp. 706–727, 2nd ed.
  - <sup>37</sup> M. Usuda, J. Igarashi, and A. Kodama, *Phys. Rev. B* **69**, 224402 (2004).
  - <sup>38</sup> Orbital polarization here is concerned with the orbital angular momentum.